Available online at www.sciencedirect.com
ScienceDirect
Journal of Nuclear Materials 371 (2007) 134–144
journal of nuclear materials
www.elsevier.com/locate/jnucmat

Time dependence of corrosion in steels for use in lead-alloy cooled reactors

McLean Machut [a,*], Kumar Sridharan [a], Ning Li [b], Shigeharu Ukai [c], Todd Allen [a]

[a] *Department of Nuclear Engineering and Engineering Physics, University of Wisconsin-Madison, 1500 Engineering Dr., Madison, WI 53706, United States*
[b] *Materials Physics and Application Division, AFCI, Los Alamos National Laboratory, NM, United States*
[c] *Division of Materials Science and Engineering, Hokaido University, Japan*

Abstract

Stability of the protective oxide layer is critical for the long-term performance of cladding and structural components in lead-alloy cooled nuclear systems. Measurements have shown that removal of the outer magnetite layer is a significant effect at higher temperatures in flowing lead–bismuth. Developing a predictive capability for oxide thickness and material removal is therefore needed. A model for the corrosion of steels in liquid lead-alloys has been employed to assist in materials development for application in the Generation IV Lead-cooled Fast Reactor (LFR). Data from corrosion tests of steels in Los Alamos National Laboratory's DELTA Loop is used to benchmark the model and to obtain predictions of long-term material's corrosion performance. The model is based on modifications of Wagner's diffusion based oxidation theory and Tedmon's equation for high-temperature oxidation with scale removal. Theoretically and experimentally obtained values for parabolic oxide growth rate, mass transfer corrosion rate, and long-term material thinning rates are presented and compared to the literature.

---

1. Introduction

1.1. Corrosion in a liquid lead-alloy environment

Liquid lead-alloys possess many desirable qualities for use as coolant in advanced nuclear reactors like the Generation IV Lead-Cooled Fast Reactor concept (LFR). Some of these characteristics include favorable heat transfer, fluid dynamics, and neutronic performance compared to other candidate coolants. However, a significant challenge facing the LFR is the selection and development of structural and cladding materials suitable for long-term use in the highly corrosive liquid metal environment [1]. Corrosion in a liquid lead-alloy can manifest itself in several forms including dissolution, compound formation, and liquid metal penetration along grain boundaries. Several factors contribute to these corrosion mechanisms, including, temperature and thermal gradient, exposure time, flow rate, coolant chemistry, material compositions, and in particular the oxygen content of the melt. Studies also suggest a minimum Cr alloying content is required in the steels for the formation of a protective oxide layer. Ferritic/martensitic

---

[*] Corresponding author. Fax: +1 608 262 7451.
E-mail address: mtmachut@wisc.edu (M. Machut).

0022-3115/$ - see front matter © 2007 Elsevier B.V. All rights reserved.
doi:10.1016/j.jnucmat.2007.05.009

(FM) steels, with low bulk nickel concentrations, have a marked advantage over austenitic steels and Ni-based alloys for long-term applications because the relatively high solubility of Ni in liquid lead-alloys can lead to higher material loss rates for austenitic steels and Ni-base alloys. Ferritic/martensitic steels also have superior resistance to radiation-induced dimensional changes.

To facilitate component lifetime predictions, a physically based model that describes long-term corrosion is required. This work employs a proposed model as an initial basis for corrosion prediction and compares the model to measurements of oxide growth of materials exposed to lead bismuth eutectic (LBE) at high temperatures. The proposed model is based on the assumption that there are two kinetic processes in competition: (1) oxidation by simultaneous inward diffusion of oxygen and outward metal ion diffusion and (2) oxide scale removal from the steel surface into the flowing lead-alloy environment [2]. Since these two processes have opposite effects on the oxide thickness, there will be a limiting oxide thickness (δ_c) which can be determined based on the diffusion rates of the species through the surface layers and the removal rate at the surface. Such a model should ultimately be able to explain the oxidation behavior observed in this and previous studies, arriving at a comprehensive model to predict corrosion in a flowing lead-alloy environment.

This paper will first introduce the experiments and data which provided the impetus for these modeling studies and will be used to benchmark theoretical calculations. The experimental results will be followed by a brief review of the underlying theory and methodology for the physical and theoretical models. Finally, the results of theoretical calculations as well as experimentally obtained benchmarks and comparisons to the literature are presented.

2. Corrosion experiment

The literature describes many attempts to understand the fundamental corrosion mechanisms of steels in liquid lead-alloys at temperatures up to 550 °C where they might be useful in application to an LFR [2,8,14]. The present study involved three candidate alloys under consideration for the LFR environment: NF616, a nominal 9% chromium steel; HCM12A, a nominal 12% chromium steel; and a 9Cr oxide dispersion strengthened (ODS) steel. NF616 and HCM12A are third generation ferritic–martensitic steels designed for high-temperature fossil boiler components that are being evaluated for nuclear application. The ODS steel exhibits remarkable strength even at temperatures as high as 750 °C due to the presence of a fine dispersion of nanometer sized particles of yttrium–titanium-oxide and a resulting grain structure that is much finer than that of the other steels. The steel specimens for this research were prepared in the form of precisely machined $8 \times 35 \times 1$ mm coupons polished using successively finer grits of SiC grinding paper and finished with colloidal silica to achieve a mirror-like finish. Compositions of the steels investigated in this research are listed in Table 1.

Exposure of these alloys to molten lead–bismuth eutectic environment at 530 °C was carried out in the DELTA Loop at the Los Alamos National Laboratory. The molten alloy flow velocity in the loop was 1.2 m/s and oxygen sensors were used to measure and maintain an oxygen concentration at about 1×10^{-6} wt%. Samples were exposed for 200, 400, and 600 h to study early stages of oxide formation and growth.

2.1. Results

Characterization of exposed samples was carried out by scanning electron microscopy (SEM) with both secondary and backscattered electron imaging (SEI, BEI). Examination was made both in surface plan view and in cross-section and analyzed with energy dispersive X-ray spectroscopy (EDS) in the form of elemental composition maps, line scans, and surface spectra.

Table 1
Composition by wt% of alloys tested, balance Fe

	Cr	Ni	Mo	Mn	W	Si	V	Nb	Ti	C	O	N	Cu	Y	Y_2O_3
HCM12A	10.83	0.39	0.30	0.64	1.89	0.27	0.19	0.054	–	0.11	–	0.063	1.02	–	–
NF616	8.82	0.174	0.468	0.45	1.87	0.102	0.194	0.064	–	0.109	0.0042		–	–	–
ODS	8.67	0.06	–	0.05	1.95	0.05	–	–	0.23	0.14	0.14	0.017	–	0.28	0.35

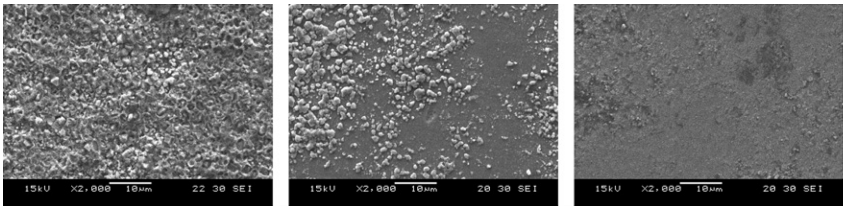

Fig. 1. Secondary SEM surface micrographs of 200, 400, and 600 h exposed (530 °C) HCM12A samples showing how eventual removal of Fe-oxide particles reveals protective Cr-rich oxide layer.

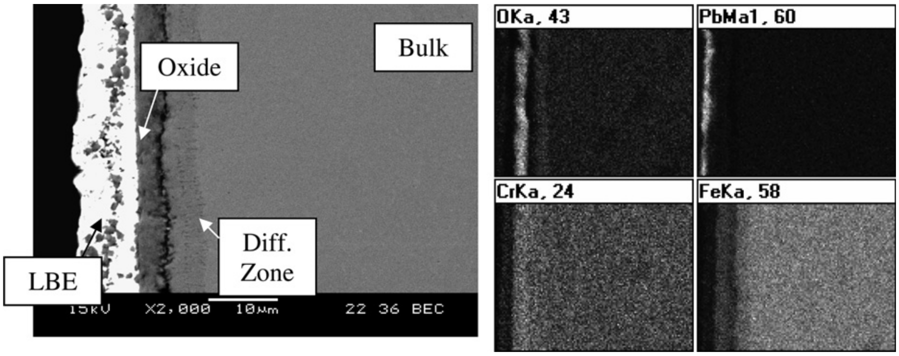

Fig. 2. HCM12A samples show Cr-rich oxide and diffusion zone in a backscatter cross-section SEM image (left) after 400 h of exposure and an EDS map (right) after 600 h at 530 °C.

2.1.1. HCM12A

The surface and cross-section SEM/EDS of the HCM12A samples show the early formation of iron oxide (Fe_3O_4, magnetite) particles on the surface, which are eventually carried away by the LBE to reveal a much smoother underlying Cr-rich oxide layer ($(Fe,Cr)_3O_4$) and a diffusion zone underneath (see Figs. 1 and 2). By contrast, the same alloy tested at 460 °C in previous experiments [15] had the outer magnetite layer still intact even after 1000 h, with a Fe–Cr spinel layer underneath. Hence the increased temperature, which corresponds with faster diffusion rates, decreases the amount of time it takes to form a uniform protective Cr-rich spinel and to remove the outer magnetite. The thickness of the spinel layer remains relatively constant after 200 h at 530 °C, although the thickness of the diffusion layer continues to increase.

2.1.2. NF616

Surface SEM images of NF616 show a similar trend of Fe-oxide particle removal to reveal a smoother (though less so than HCM12A) surface after 600 h. However, the cross-section images display a thicker oxide and a much thinner diffusion zone (see Figs. 3 and 4). The diffusion zone is not visible at all after a 200 h exposure (not shown). For NF616, the outer layer of Cr-rich spinel grew slightly while the inner diffusion zone stayed constant after 400 h. The differences in oxidation mechanism may be related to the smaller amount of Cr relative to HCM12A.

2.1.3. ODS steel

For the 9Cr-ODS steel, the magnetite has already been removed to reveal a very smooth surface after only 400 h. ODS exhibits the reverse trend compared to NF616 in that the spinel is now much thinner while the diffusion zone is thicker (see Figs. 5 and 6). Although Cr content is similar to NF616, an increased removal rate of the outer oxide occurs on the much finer grained ODS steel.

2.1.4. Summary of experimental results

At short times, the steels formed a protective duplex oxide layer consisting of an outer magnetite (Fe_3O_4) layer and an inner Fe–Cr spinel ($(Fe,Cr)_3O_4$) layer which is sometimes accompanied by an O-enriched and Fe-depleted diffusion zone at the oxide–bulk interface. With time, the outer magnetite layer is removed by the melt and the

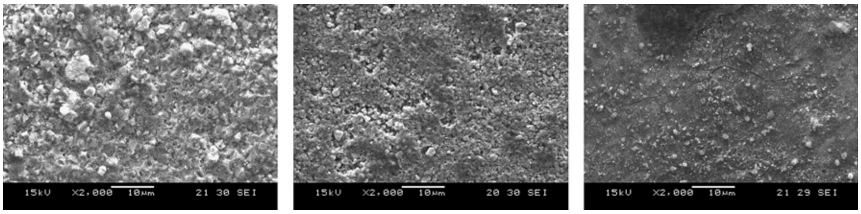

Fig. 3. Secondary SEM surface micrographs of 200, 400, and 600 h exposed (530 °C) NF616 samples again showing how eventual removal of Fe-oxide layer particles reveals protective Cr-rich oxide layer.

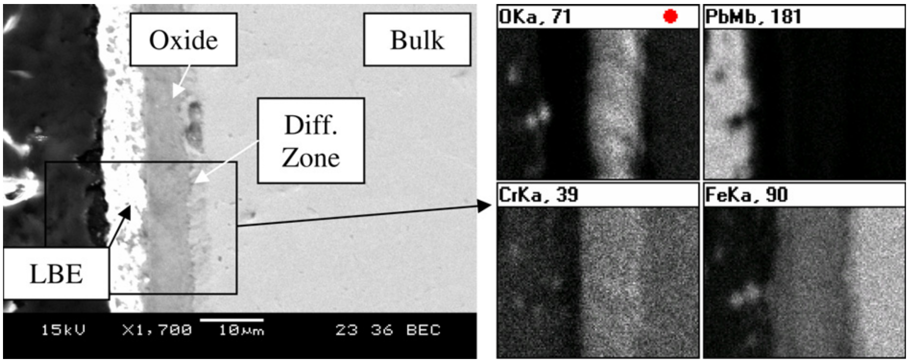

Fig. 4. Relative to HCM12A, the NF616 samples show a thicker Cr-rich oxide layer and a thinner diffusion zone in a backscatter cross-section SEM image (left) after 400 h of exposure and an EDS map (right) after 600 h at 530 °C.

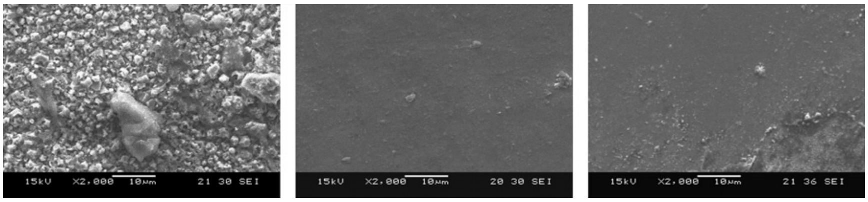

Fig. 5. Secondary SEM surface micrographs of 200, 400 and 600 h ODS samples showing how, already at 400 h, removal of Fe-oxide layer reveals protective Cr-rich oxide layer.

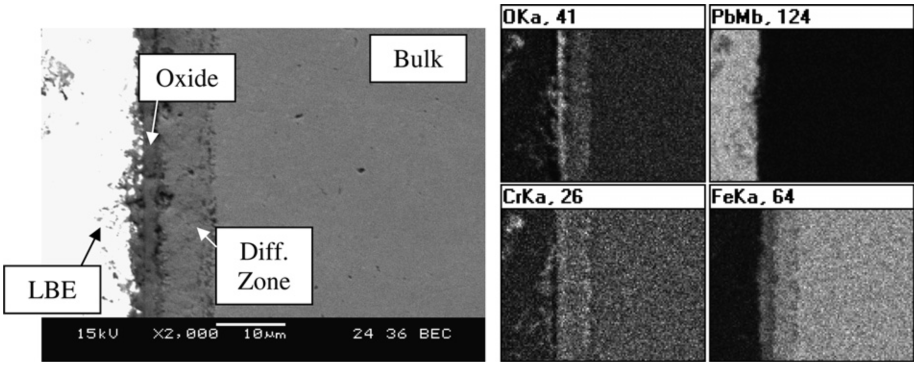

Fig. 6. Backscatter cross-section SEM image and EDS map of 600 h ODS sample showing much thinner Cr-rich oxide but a thicker diffusion zone.

Table 2
Oxide thicknesses in microns vs. time for 530 °C LBE exposure

Alloy	Hours	Oxide layer	Diff. zone	Total
HCM12A	200	4.46	2.98	7.44
	400	4.42	4.83	9.25
	600	4.93	5.21	10.14
NF616	200	5.92	0.00	5.92
	400	6.66	3.70	10.36
	600	7.31	2.35	9.66
ODS	200	2.47	5.43	7.90
	400	4.61	5.92	10.53
	600	2.14	7.86	10.00

underlying spinel layer serves to mitigate more catastrophic corrosion degradation such as dissolution and liquid metal attack along grain boundaries. Very thin oxides are not particularly protective in regards to loss of metal, as manifested by thick diffusion zones associated with them. The oxide layer (magnetite plus spinel) and diffusion zone thicknesses vs. time are shown in Table 2.

It is important to point out that these experiments are the first known observation of removal of the outer magnetite layer within such a short period of time. Models presented by Zhang and Li had predicted such a trend but not for much longer timeframes [5]. Therefore, a theoretical model based on the same framework used by Zhang and Li has been reworked and applied to these novel experimental results in attempt to explain differences in experimental data and to improve upon the predicative capabilities of existing models.

3. Theory

3.1. Protective oxide scale formation

The in situ formation of a protective oxide scale on the surface of the steel provides the ultimate corrosion barrier for materials to be used in high temperature, oxidizing environments. To ensure that the scale formed is indeed protective in nature, there are several key requirements for the system [3]:

(1) Thermodynamic stability – The protective oxide must be thermodynamically more stable than oxides of lead or bismuth at the temperatures and oxygen concentration of the system.
(2) Low diffusion – Limited movement of species through the oxide phases favors growth at the interface of various phases/regions which is inversely proportional to scale thickness. This leads to dense, compact oxides with parabolic growth characteristics.
(3) Low scale-removal rate – If removal of the oxide scale by one of a number of mechanisms including volatilization, dissociation, mass transfer corrosion, or erosion is fast compared to oxide growth then there will be little or no protection from the oxide film.
(4) Mechanical integrity – To remain adherent for long periods of time, the equilibrium thickness of the oxide must be less than the critical thickness at which the mechanical integrity is compromised.

There are several other requirements which may be important but will not be specifically addressed in this research. The scale must have adequate resistance to contaminants and impurities in and around the oxide scale as well as be impermeable to aggressive components such as nitrogen, sulfur, and carbon which may contribute to internal corrosion. For a nuclear system, the scale must also retain the aforementioned properties under irradiation. Lastly, there are several approaches to surface treatment (surface alloying, coatings, pre-oxidation, etc.) that can assist in the formation of more protective oxide.

3.2. Physical model for complex oxide formation

The classical treatment of complex oxidation of binary alloys (i.e. Fe–Cr) first developed by Wagner [6] will be used to describe the oxidation behavior of the ferritic–martensitic steels under consideration for application in an LFR system. The duplex oxide that is typically formed in steels at high temperatures is due to the difference in thermodynamic stability and diffusion rates of iron and chromium. In an Fe–Cr–Pb–Bi–O system, the Cr-oxides have more negative free energies and one would expect them to form the first layers in a complex oxide structure. However, since the concentration of Cr at the surface is low, it is expected that formation of a pure chromia (Cr_2O_3) layer is unlikely. Thermodynamic stability then predicts the $(Fe,Cr)_3O_4$ spinel and the Fe_3O_4 magnetite as the most likely oxide layers to be formed on the surface of steels at temperatures below ~570 °C. At temperatures above 570 °C FeO (wustite) forms preferentially [8]. The diffusion region which rests between the inner spinel and the bulk steel is likely the result of an increase in cation vacancies due to the outwards diffusion of iron through the oxide layers and is accompanied by additional inwards oxygen diffusion that does not yet result in complete oxidation. It appears that the removal rate of Fe_3O_4 is significantly greater than that of the spinel, resulting in full removal after a relatively short period of time at 530 °C. A schematic of the physical mechanisms that must be incorporated into a corrosion model is shown in Fig. 7.

The schematic illustrates the diffusion of various species through the complex oxide layers formed and provides a basis for constructing the corrosion model. The inner oxide layer, enriched in Cr, serves as the ultimate protective oxide layer. Oxidation is driven by diffusion of iron (and chromium to a lesser extent) cations out of the diffusion zone in the bulk through the oxide layers and simultaneous inwards diffusion of oxygen through the oxide layers to the diffusion zone. The magnetite/spinel interface lies at the original liquid/metal interface. Based on this physical model and the known diffusion behavior of various species, a prediction can be made about the Fe, Cr, and O concentrations in the various layers. One would expect the oxygen content to be the greatest in the oxide layers and drop off through the diffusion zone to zero in the bulk [9]. Chromium should be nearly nonexistent in the outer layer, greatest in the spinel layer, and back to the alloy concentration in the bulk. Lastly, iron should be prevalent in the outer layer but be suppressed in the spinel and diffusion zone before rising back to its alloy concentration in the bulk. An EDS line scan along the cross-section of an HCM12A sample exposed at a lower temperature (460 °C, at which magnetite removal is not observed) demonstrates these trends (see Fig. 8).

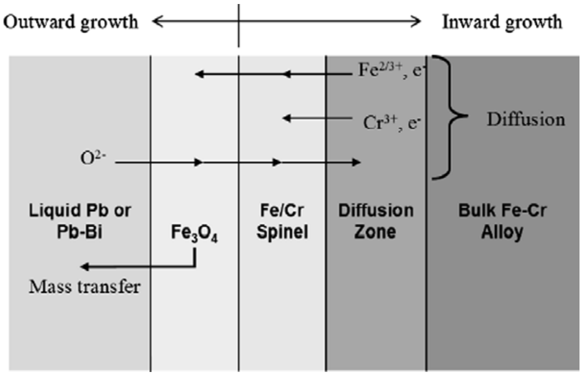

Fig. 7. Schematic illustration of corrosion mechanisms.

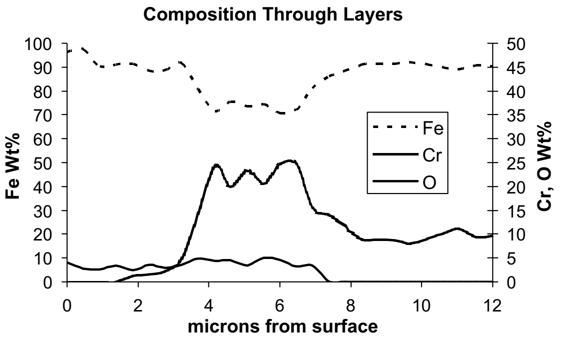

Fig. 8. Fe, Cr, and O content through oxide layers of HCM12A exposed to LBE at 460 °C.

3.3. Tedmon's equation and rate constants

The duplex oxide structure found in our experimental results is predicted by thermodynamics and Wagner's diffusion theory and is not unique to the lead-alloy environment. However, the removal of the outer oxide (in this case by the flowing LBE) is not as commonly seen. When oxide layers experience simultaneous growth and removal, a more appropriate treatment for the oxide growth rate, based on Tedmon's equation [4] (Eq. (1)) which was first used to describe scale volatilization of Cr-oxide, can be examined:

$$\frac{\mathrm{d}\delta}{\mathrm{d}t} = \frac{K_\mathrm{p}}{2\delta} - K_\mathrm{r}, \tag{1}$$

where δ is the oxide thickness, t is time, K_p is the parabolic oxide growth rate constant and K_r is the linear scale removal rate constant. Solving for oxide thickness in time yields asymptotic behavior where the thickness will approach some limiting thickness δ_c regardless of initial thicknesses (Eq. (2), [5]):

$$\delta\ (t \to \infty) = \delta_\mathrm{c} = \frac{K_\mathrm{p}}{2K_\mathrm{r}} \quad (\mu\mathrm{m}). \tag{2}$$

This solution assumes that the limiting thickness is less than the critical thickness for mechanical breakdown. Zhang and Li [5] extend the solution to weight change over time, where a maximum weight gain will be realized during an initial growth dominated period followed by what eventually becomes a linear material loss rate in the latter removal-dominated period. An expression for the long-term material thinning rate based on the scale removal rate (K_r), densities of the oxide and steel $(\rho_{\mathrm{M}_x\mathrm{O}_y}, \rho_\mathrm{M})$

and mass fraction of oxygen in the oxide (F_O) follows (Eq. (3), [5]):

$$R_r = \frac{\rho_{M_xO_y}}{\rho_M}(1 - F_O)K_r \quad (\mu m/yr). \tag{3}$$

This calculated loss rate (R_r) is an important parameter in determining material lifetime in a lead-alloy cooled reactor environment and provides a useful metric with which to compare materials. In summary, the analysis based on Tedmon's equation provides a means for assessing the long-term performance of materials if the growth and removal rate constants are known. To determine the rate constants, an effort is made to apply theory and experimental data to build a comprehensive model for the overall corrosion behavior.

3.3.1. Determining growth rate constant

Wagner's treatment is valid for diffusion-limited, high-temperature, compact scale formation. In Wagner's treatment, oxidation proceeds by cation (Fe and Cr) diffusion from the bulk metal to the surface and oxygen anion diffusion from the environment into the bulk metal, and the reactions at phase boundaries are assumed to be relatively rapid [7]. The result is a parabolic oxide growth rate constant K_p that is dependant on diffusion coefficients of metal cations (D_m) and oxygen anions (D_O) and partial pressures of oxygen at the scale interfaces (Eq. (4), [2]):

$$K_p = \int_{(P_{O_2})II}^{(P_{O_2})I} (\alpha D_m + D_O)\,d\ln P_{O_2}, \tag{4}$$

where α is the oxygen/metal atom ratio (i.e. 4/3 for magnetite) and I and II represent the oxide/bulk and oxide/LBE interfaces, respectively. The oxygen partial pressures at the interfaces can be set to the dissociation oxygen partial pressure of the oxides that are formed [9], but the diffusion coefficients must be determined.

3.3.2. Diffusion

The relative difference in diffusion rates of iron and chromium are important in driving the formation of the complex oxide. Because the diffusion of chromium through bulk alloys and oxides is much slower than that of iron [9], Cr can be treated as relatively immobile compared to Fe. Thus, while Fe cations are free to move through the inner spinel layer and form the pure iron oxide at the original bulk/LBE interface, oxidation of iron and chromium also progresses inward via diffusion of oxygen from the molten LBE environment through the oxide layers. Recalling the second protective oxide requirement from Section 2.1, diffusion of oxide molecules is considered negligible such that the movement of Fe cations and oxygen anions are the rate limiting events. Hence, the next logical step in the development of the corrosion model is to determine diffusion coefficients for Fe/Cr and O through the bulk alloy and oxide layers. These oxidation mechanisms will be revisited after comparison to experimental results.

The radiotracer-derived Arrhenius correlation from Castle and Surman for oxygen in magnetite under similar oxygen partial pressures and temperatures that was used for the calculations in this study is shown here (Eq. (5), [10]):

$$D_O = 3.2 \times 10^{-10} \exp\left(-\frac{17\,000}{RT}\right) \quad (m^2/s). \tag{5}$$

Use of this correlation assumes a dense, compact oxide scale, whereas the actual oxygen diffusion rates can be accelerated due to porosity or cracks in the oxide layer. As will be seen below, using the above diffusion coefficient still allowed for reasonable correlation between model and measurements.

Cation diffusion requires further consideration owing to the several mechanisms by which diffusion can take place in the oxide, all of which are highly dependant on the nature of the oxide itself. The cation diffusion coefficient in the oxide was determined by using a combination of correlations that account for both lattice diffusion and grain boundary diffusion while adjusting for grain size and oxide density. Diffusion can occur via migration of point defects in the lattice structure or via fast diffusion pathways such as grain boundaries and dislocations. The concentration of point defects depends largely on non-stoichiometry and impurities in the oxide structure while fast pathways are dependant on grain size and mechanical stresses. The correlation developed by Dieckmann and Schmalzried (Eq. (6), [2]) used to account for vacancy (D_V^0) and interstitial (D_I^0) point defect diffusion in magnetite is

$$D_m = \left(D_V^0 \exp\left(-\frac{138\,600}{RT}\right) + D_I^0 \exp\left(-\frac{614\,200}{RT}\right)\right) P_{O_2}^{-2/3} \quad (m^2/s), \tag{6}$$

where values for vacancy (D_V^0) and interstitial (D_I^0) diffusion coefficients were found experimentally to be 4×10^{-15} m^2/s and 8×10^3 m^2/s, respectively. Diffusion via point defects through the bulk spinel grains is not expected to vary much from magnetite due to similarity in bulk grain lattice structure. Since the point defect model is expected to underestimate the diffusion coefficients because the fast pathway diffusion is not appropriately represented, a simple correction can be made based on grain size of the oxide scale measured via EBSD technique (Eq. (7), [11]). The *Oxide Handbook* [12] reports a correlation for grain boundary (D_{gb}) diffusion (Eq. (7), [10]):

$$D_{gb} = 1.27 \times 10^{-3} \exp\left(-\frac{151\,562}{RT}\right) \quad (\mathrm{m^2/s}) \tag{7}$$

such that an effective diffusion rate $D_{m,eff}$ may be calculated for cations through the scale using the following (Eq. (8), [2]):

$$D_{m,eff} = D_m(1-\Phi) + D_{gb}\Phi, \quad \Phi = \frac{2\varepsilon}{g}, \tag{8}$$

where Φ signifies the fraction of fast pathway diffusion sites and can be approximated by treating grains as rectangular prisms with height and width g and length ε (comes to about 0.96 using measurements from a study by Tan et al. [11] for HCM12A at 530 °C). The final estimate for cation diffusion in the oxide was thus determined by using Eqs. (7) and (8) to adjust the result from the point defect model (Eq. (6)).

3.4. Mass transfer corrosion

Zhang and Li proposed a model for the mass transfer corrosion at the solid-liquid interface [13]. This approach relates the difference in concentrations of species at the interface and in the bulk to a mass transfer coefficient k_m (Eq. (9), [13]):

$$R_m = k_m(c_s - c_b) \quad (\mu\mathrm{m/yr}). \tag{9}$$

The concentration of iron at the oxide surface (c_s) is calculated based on a correlation from Sannier and Santarini in pure lead (Eq. (10), [13]):

$$\log(c_s) = \left(4.34 - \frac{3450}{T(\mathrm{K})}\right) \quad (\mathrm{ppm}) \tag{10}$$

and the bulk concentration (c_b) is negligible for the short times in this study. The calculated mass transfer corrosion rate R_m can then be calculated and compared to the measured removal rate R_r. The mass transfer corrosion rate constant k_m can be calculated analytically by the following expression developed for mass transfer in fluid flow derived by Zhang and Li (Eq. (11), [13]):

$$k_m = \frac{3}{2\Gamma\left(\frac{1}{3}\right)}\left(\frac{3}{1740}\right)\upsilon^{-2/3}D^{2/3}V\left(\frac{\lambda}{2}\right)^{1/2}, \tag{11}$$

where υ is the kinematic viscosity, V is the flow velocity, λ is the Fanning friction factor, and D is the diffusion coefficient for iron in lead, for which the following correlation found by Robertson was used (Eq. (12), [2]):

$$D_{\mathrm{Fe}\to\mathrm{Pb}} = 4.9 \times 10^{-7} \exp\left(-\frac{44\,100}{RT}\right) \quad (\mathrm{m^2/s}). \tag{12}$$

Substituting for the Gamma function ($\Gamma(1/3) = 2.6789$) and using the well-known Blasius correlation for turbulent flow ($\lambda = .0791\mathrm{Re}^{-.25}$) in Eq. (11) yields the following simplification, where d is the hydraulic diameter (Eq. (13), [13]):

$$k_m = .0133\upsilon^{-.542}D^{.667}V^{.875}d^{-.125}. \tag{13}$$

4. Modeling and benchmarking results

4.1. Theoretical results

4.1.1. Parabolic rate constant

The rate constant calculation follows using the previously discussed methods (Section 2) at 530 °C. The oxygen partial pressures were set to approximate values for oxide dissociation at the boundaries (@530C, $\sim 1 \times 10^{-27}$ for Fe_3O_4 oxide dissociation at the liquid/oxide interface and $\sim 5 \times 10^{-31}$ for the oxide/diffusion zone interface). The value of the partial pressure at the oxide/diffusion zone is higher than the dissociation partial pressure of $(Fe,Cr)_3O_4$ because the selective oxidation clearly extends into the metal and is expected to follow an exponential decay law through the internal oxidation layer [9]. It should be noted that the diffusion coefficients are highly sensitive to these P_{O_2} estimates. This said, the corrections made by adjustments for diffusion mechanisms and grain size above have relatively little effect in determining the order of magnitude for the diffusion coefficient, but are useful in estimating relative differences between differing oxide properties. The calculated diffusion coefficients using Eqs. (5)–(8) are calculated to be 1.43×10^{-13} m^2/s for the cation diffusion coefficient and 2.51×10^{-15} m^2/s for the anion diffusion coefficient. The final parabolic growth rate was

Table 3
Comparison of theoretical growth rate constants

	K_p (m^2/s)
This study	1.16E−16
Zhang and Li	3.21E−17
Saito et al.	4.75E−18
Smith et al.	2.64E−17

about an order higher in magnitude than reported calculated values from previous studies by Zhang and Li, Saito et al., and Smith et al. at 550 °C [2], and all are presented in Table 3 for comparison.

The reasons for this discrepancy likely lies in a difference in the diffusion coefficients used, since certain correlations used may underestimate overall diffusion rates. It will be seen later that the higher value for the growth rate constant agrees better with the experimental results of this work.

4.1.2. Scale removal rate constant

A number of assumptions about the system flow parameters must be made for the calculation of mass transfer corrosion rate. The input values for Eqs. (9) and (13) used for the removal rate calculation were: calculated iron diffusion coefficient in lead of 6.55×10^{-10} m^2/s (Eq. (12)), experimental flow velocity of 1.2 m/s, experimental temperature of 530 °C, dynamic viscosity of 1.33×10^{-7} m^2/s [13], experimental hydraulic diameter of .01 m, and saturation concentration (c_s) of 7.68×10^{-8} g/m^3 with negligible bulk concentration (c_b) [13]. Using the calculated result for R_m (Eq. (9)) as the thinning rate R_r in Eq. (3) to obtain a value for K_r gives 2.03×10^{-12} m/s, compared to a value of 9.10×10^{-13} m/s calculated by Zhang and Li at 550 °C [2]. This corresponds to a long-term thinning rate of about 37.6 μm/yr (12.7 from Zhang and Li). The reason for the higher estimate despite a slightly lower temperature is due to different assumptions for the hydraulic diameter and flow velocity parameters in the mass transfer corrosion model; this study examines an individual sample holder channel whereas Zhang and Li's calculations are for the larger piping of the Delta loop (hydraulic diameter ~2.5 cm) [13].

4.2. Comparison with experimental results

4.2.1. Early stage kinetics

The total (oxide layer plus diffusion zone) thickness data from the test is fit using a least squares method to the early stage kinetic approximation for the Tedmon model as in the treatment by Zhang et al. [5] which give Eq. (14) for oxide thickness δ:

$$\delta = (K_p t)^{(1/2)} - \frac{2}{3} K_r t, \tag{14}$$

where K_p again is the growth rate constant, t is time, and K_r is the removal rate constant. The experimental results were fitted to Eq. (14) using a least squares technique to obtain values for K_p and K_r and are plotted in Fig. 9 along with the measured total thickness (oxide plus diffusion zone) data from the 530 °C test.

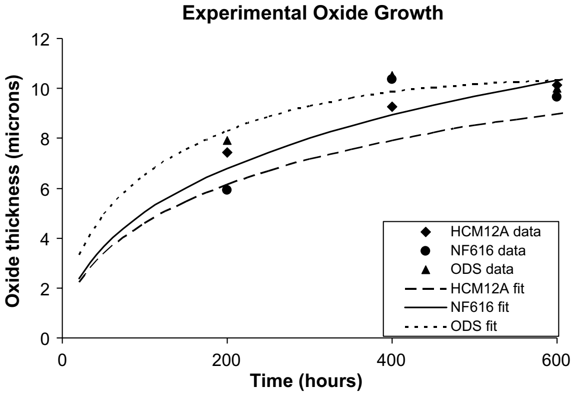

Fig. 9. Experimental early-stage oxide growth results.

Eq. (14) can also be used to plot the oxide thickness calculated using the growth and removal rate constants derived from Eqs. (3), (4), (9), and (13) (Fig. 10), showing excellent agreement with the experimental data:

The experimentally obtained values for the growth rate constant K_p and the removal rate constant K_r from the least squares fitting are listed in Table 4 along with the corresponding calculated

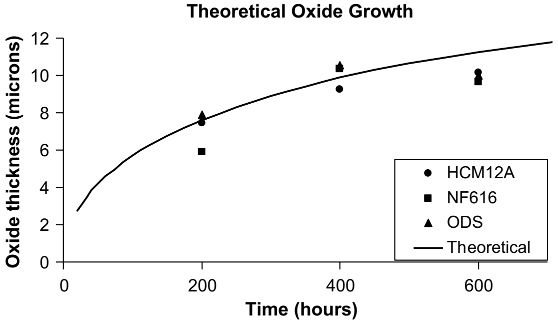

Fig. 10. Theoretical values for oxide growth using early stage kinetics with total thickness data from the 530 °C test.

Table 4
Tedmon's equation fitting results for experimental data

	K_p (m^2/s)	K_r (m/s)	R_r (μm/yr)	δ_c
HCM12A	1.27(±0.2)E−16	4.45(±0.6)E−12	43.2(±5.7)	14.3(±0.4)
NF616	8.63(±1.4)E−17	2.31(±0.6)E−12	22.4(±5.5)	18.7(±1.0)
ODS	1.84(±0.3)E−16	6.70(±0.6)E−12	65.1(±5.4)	13.8(±0.6)
HT9, Zhang and Li	1.48E−16	1.01E−13	14.0	73.6
D9, Zhang and Li	6.87E−17	7.04E−13	9.8	48.8

values for removal rate R_r (using Eq. (3)) and limiting thickness δ_c (using Eq. (2)). For comparison, fitting results from two alloys in a longer (3000 h, 550 °C) Zhang and Li study [2] are included.

Both the parabolic growth rate constants and the mass transfer removal rate constants are on the order of those predicted by the model. The removal rate for HCM12A is within error of the 37.6 μm/yr predicted by the theoretical calculation, whereas NF616 is slightly less and ODS is somewhat higher. The limiting thicknesses of around 15 μm agree well with those observed in the corrosion experiments, especially compared to those predicted by Zhang and Li which are much larger than has been seen experimentally. In summary, faster overall thinning rates and thinner limiting oxide thicknesses are predicted compared to the results of Zhang and Li, just as with the theoretical calculations.

5. Conclusions

A model has been adapted to understand important mechanisms of complex oxide formation and removal for 9–12Cr ferritic martensitic steels in molten lead-alloy coolant. The model can estimate the early stage kinetics for the complex scale as well as long-term materials thinning rate under the assumption that the scale is within its mechanical stability limits so that the protective oxide scale (in this case, the Fe–Cr spinel) remains intact and adherent. Tedmon's equation, Wagner oxidation theory, and mass transfer corrosion theory have provided theoretical values for growth and removal rate constants for the oxide scale. Experimental data has been used to benchmark the calculated values; The parabolic oxide growth rate constant was determined to be on the order of 1×10^{-16} m^2/s, and the scale removal rate constant on the order of 2×10^{-12} m/s, leading to long-term material loss rate of about 40 μm/yr. For a 20 year application, as is proposed by current LFR designs, this translates to nearly 1 mm. While this may be within design limits for certain structural materials, potential cladding materials would be on the order of 1 mm, indicating that other techniques such as surface treatments or pre-oxidation may be necessary to meet cladding materials requirements [15]. It is also interesting to see that while the limiting oxide thickness may vary from alloy to alloy, the long-term material thinning rate is fairly consistent. This means that measurement of the total oxide thickness at a given time is not necessarily the best metric for predicting corrosion performance of a particular material. Rather, the growth and removal processes most both be accounted for over time to accurately asses the corrosion performance. Furthermore, future modeling work including better long-term (>5000 h) materials performance estimates and experimental weight gain measurements will allow for the development of a superior evaluation technique. Additional recommendations for future studies would include examination of the overall durability and impermeability of the protective spinel layer once the outer magnetite is removed and incorporation of the internal oxidation layer to the model. Finally, improvements to the input parameters for the theoretically obtained parabolic growth and removal rate constants, particularly those to which the calculation is particularly sensitive such as the partial pressure of oxygen at the interfaces, would further reinforce and validate the model.

Disclaimer

its endorsement, recommendation, or favoring by the United States Government or any agency thereof. The views and opinions of authors expressed herein do not necessarily state or reflect those of the United States Government or any agency thereof.

Acknowledgements

This material is based upon work supported by the US Department of Energy under the NEER program Award No. DE-FG07-04ID14600 and NEER Project Number 81.114. Special thanks to Drs Lizhen Tan of UW and Jinsuo Zhang of LANL and for their valuable contributions to this work.

References

[1] T. Allen, R. Klueh, N. Li, Initial Generation IV Reactors Integrated Materials Technology Program Plan, ORNL/TM-2003/244, 2003.

[2] J. Zhang, N. Li, Oxid. Met. 63 (5–6) (2005).

[3] M. Schutze, Protective Oxide Scales and Their Breakdown, John Wiley, New York, 1997.

[4] C.S. Tedmon, J. Electrochem. Soc. 142 (1967).

[5] J. Zhang, N. Li, Y. Chen, J. Nucl. Mater. 342 (1–3) (2005).

[6] C. Wagner, J. Electrochem. Soc. 99 (10) (1952).

[7] P. Kofstad, High Temperature Oxidation of Metals, John Wiley, New York, 1966.

[8] F. Barbier, A. Rusanov, J. Nucl. Mater. 296 (2001) 231.

[9] Y. Matychak, V. Pavlyna, V. Fedirko, Mater. Sci. 39 (5) (2003).

[10] J.E. Castle, P.L. Surman, J. Phys. Chem. 71 (13) (1967).

[11] L. Tan, M. Machut, K. Sridharan, T. Allen, in: ANS Meeting: Nuclear Fuels and Structural Materials for the Next Generation Nuclear Reactors, Reno, NV, June 2006.

[12] G. Samsanov (Ed.), The Oxide Handbook, Plenum, New York, 1973.

[13] J. Zhang, N. Li, Nucl. Technol. 144 (2003).

[14] T. Furukawa, G. Müller, G. Shumacher, A. Weisenburger, A. Heinzel, F. Zimmerman, K. Aoto, J. Nucl. Sci. Technol. (2004).

[15] M. Machut, K. Sridharan, N. Li, T. Allen, in: International Congress on Advances in Nuclear Power Plants, Nice, France, May 2007, paper #7221.